A three-dimensional Eulerian method for the numerical simulation of high-velocity impact problems*

Wu Shi-Yu(吴士玉)[a], Liu Kai-Xin(刘凯欣)[a,b,†], and Chen Qian-Yi(陈千一)[a]

[a] LTCS and Department of Mechanics and Engineering Science, College of Engineering, Peking University, Beijing 100871, China
[b] Center for Applied Physics and Technology, Peking University, Beijing 100871, China

(Received 12 September 2013; revised manuscript received 23 July 2013; published online 24 January 2014)

In the present paper, a three-dimensional (3D) Eulerian technique for the 3D numerical simulation of high-velocity impact problems is proposed. In the Eulerian framework, a complete 3D conservation element and solution element scheme for conservative hyperbolic governing equations with source terms is given. A modified ghost fluid method is proposed for the treatment of the boundary conditions. Numerical simulations of the Taylor bar problem and the ricochet phenomenon of a sphere impacting a plate target at an angle of 60° are carried out. The numerical results are in good agreement with the corresponding experimental observations. It is proved that our computational technique is feasible for analyzing 3D high-velocity impact problems.

Keywords: three-dimensional numerical simulation, conservation element and solution element (CE/SE) method, ghost fluid method, high-velocity impact

PACS: 46.15.–x, 62.20.mm, 64.30.Ef **DOI:** 10.1088/1674-1056/23/3/034601

1. Introduction

The study of three-dimensional (3D) high-velocity impact problems[1] is important in the design of protective structures such as armored vehicles and military bunkers. Numerical analysis plays an important role in high-velocity impact problems as it enables researchers to obtain important information that cannot be captured experimentally, such as the pressure, strain rate and porosity evolution inside the target during testing. The computer codes can be roughly classified as Eulerian (e.g. CSQ and CTH) and Lagrangian (e.g. TOODY, EPIC and DYNA) descriptions, depending on whether the material flows through a fixed mesh or the mesh follows the deformation of the solid. Lagrangian schemes work well at multimaterial interfaces, but suffer problems with large deformation;[2] an extreme case being that the simulation fails when a grid cell folds over itself. In recent decades, many Lagrangian meshless/meshfree and particle methods[3] have been proposed to solve the problems with large deformations. However, these methods have some intrinsic limitations, including a lower computing speed than other modern grid-based methods and difficulties in boundary condition treatments. Meanwhile, by allowing the boundaries to flow through a fixed mesh while computing the flow field on the fixed mesh, Eulerian codes can solve arbitrarily large distortions. Therefore, if combined with efficient numerical methods for describing moving interfaces, the Eulerian methodology is a promising alternative.

Extensive literature exists on the Eulerian methodology for high-velocity impact problems. Udaykumar *et al.*[4] presented a technique for the numerical simulation of a high-speed multimaterial impact. An accurate, high-order ENO scheme was adopted along with an interface tracking technique to evolve sharp boundaries. Subsequently, Tran and Udaykumar[5] updated their methodology by substituting the hybrid particle level set method[6] for the interface tracking algorithm. Kapahi *et al.*[7,8] proposed a 3D Eulerian, sharp interface, Cartesian grid technique to simulate the response of elasto-plastic solid materials to high-velocity impacts, shocks and detonations, and Barton *et al.*[9] developed a Eulerian adaptive numerical method for high-velocity impact problems. Wang *et al.*[10] proposed an improved space–time conservation element and solution element (CE/SE) scheme and extended it to the community of high-speed impact dynamics in solids. The CE/SE method, originally devised by Chang,[11,12] is a novel numerical scheme for solving the hyperbolic conservation laws. Chen *et al.*[13] adopted the CE/SE scheme with the hybrid particle level set method for the numerical simulation of a spall fracture due to a high-velocity impact. The CE/SE method has had great success in the field of elastic-plastic flow problems.[10,13,14]

The ghost fluid method (GFM)[15–18] was developed to capture the boundary conditions at the contact interface between two fluids, and has been extended to treat the boundary conditions at fluid–solid and solid–solid interfaces. In simulations of high-velocity impact problems in a Eulerian framework, GFM has been widely used.[4,5,7–10,13,19,20]

The present paper extends the methodology proposed by

*Project supported by the National Natural Science Foundation of China (Grant Nos. 10732010, 10972010, and 11332002).
†Corresponding author. E-mail: kliu@pku.edu.cn
© 2014 Chinese Physical Society and IOP Publishing Ltd

Chen *et al.*[13] to simulate 3D high-velocity impact problems. A more complete 3D CE/SE scheme is given for the simulation of high-velocity impact problems, containing elastic–plastic flows, high strain rates and fractures. The hybrid particle level set method[6] is adopted to capture the material interfaces, and the GFM implemented in the solid–solid interfaces is modified to treat the interface boundary conditions more efficiently. The present scheme is implemented on parallel distributed-memory computers using a domain-decomposition approach. Simulations of a Taylor bar problem and the ricochet phenomenon of a sphere impacting a plate target at an angle of 60°[21] are presented. Our numerical results are in good agreement with the experimental observations, which proves the feasibility and reliability of our computational technique.

In Section 2, we provide a detailed description of the governing equations. The 3D CE/SE scheme is then introduced in Section 3, and the interface capturing algorithm is given in Section 4. Details of the modified GFM are provided in Section 5, and in Section 6, the proposed scheme is tested by 3D impact problems. Finally, we provide a conclusion in Section 7.

2. Governing equations

Using cartesian coordinates (x, y, z), the Eulerian governing equations for the homogenous media without heat conduction, thermal diffusion and external forces can be written in the form of conservation laws as

$$\frac{\partial \boldsymbol{Q}}{\partial t}+\frac{\partial \boldsymbol{E}(\boldsymbol{Q})}{\partial x}+\frac{\partial \boldsymbol{F}(\boldsymbol{Q})}{\partial y}+\frac{\partial \boldsymbol{G}(\boldsymbol{Q})}{\partial z}=\boldsymbol{S}(\boldsymbol{Q}), \tag{1}$$

where $\boldsymbol{Q}$ is the vector of the conserved variables, $\boldsymbol{E}$, $\boldsymbol{F}$ and $\boldsymbol{G}$ are the conservation flux vectors in the x, y, and z directions, respectively, and $\boldsymbol{S}$ is the source term vector. In the Eulerian representation, these vectors are

$$\boldsymbol{Q}=\begin{bmatrix}\rho\\ \rho u\\ \rho v\\ \rho w\\ E\\ s_{xx}\\ s_{xy}\\ s_{xz}\\ s_{yy}\\ s_{yz}\\ s_{zz}\\ \varepsilon^{\mathrm{p}}\\ T\end{bmatrix},\quad \boldsymbol{E}=\begin{bmatrix}\rho u\\ \rho u^2-\sigma_{xx}\\ \rho uv-\sigma_{xy}\\ \rho uw-\sigma_{xz}\\ u(E-\sigma_{xx})-v\sigma_{yx}-w\sigma_{zx}\\ us_{xx}\\ us_{xy}\\ us_{xz}\\ us_{yy}\\ us_{yz}\\ us_{zz}\\ u\varepsilon^{\mathrm{p}}\\ uT\end{bmatrix},$$

$$\boldsymbol{F}=\begin{bmatrix}\rho v\\ \rho uv-\sigma_{xy}\\ \rho v^2-\sigma_{yy}\\ \rho vw-\sigma_{yz}\\ v(E-\sigma_{yy})-u\sigma_{xy}-w\sigma_{yz}\\ vs_{xx}\\ vs_{xy}\\ vs_{xz}\\ vs_{yy}\\ vs_{yz}\\ vs_{zz}\\ v\varepsilon^{\mathrm{p}}\\ vT\end{bmatrix},$$

$$\boldsymbol{G}=\begin{bmatrix}\rho w\\ \rho uw-\sigma_{xz}\\ \rho v^2-\sigma_{yz}\\ \rho w^2-\sigma_{zz}\\ w(E-\sigma_{zz})-u\sigma_{xz}-v\sigma_{yz}\\ ws_{xx}\\ ws_{xy}\\ ws_{xz}\\ ws_{yy}\\ ws_{yz}\\ ws_{zz}\\ v\varepsilon^{\mathrm{p}}\\ vT\end{bmatrix},\quad \boldsymbol{S}=\begin{bmatrix}0\\ 0\\ 0\\ 0\\ 0\\ S_{s_{xx}}\\ S_{s_{xy}}\\ S_{s_{xz}}\\ S_{s_{yy}}\\ S_{s_{yz}}\\ S_{s_{zz}}\\ S_{\varepsilon^{\mathrm{p}}}\\ S_T\end{bmatrix}, \tag{2}$$

where ρ is the density, u, v and w are the x, y and z components of the velocity, respectively, and E is the total energy per unit volume

$$E=\rho e+\frac{1}{2}\rho(u^2+v^2+w^2), \tag{3}$$

with e being the specific internal energy. S_{xx}, S_{xy}, S_{xz}, S_{yy}, S_{yz} and S_{zz} are the components of the deviatoric stress tensor, ε^{P} is the equivalent plastic strain and T is the temperature.

The deviatoric stress tensor S_{ij}, which obeys Hooke's law in the incremental stress form and the plasticity flow model, reflects the shear deformation. In the elastic state, the source terms of $S_{s_{xx}}$, $S_{s_{xy}}$, $S_{s_{xz}}$, $S_{s_{yy}}$, $S_{s_{yz}}$ and $S_{s_{zz}}$ in Eq. (2) can be expressed as

$$\begin{aligned}S_{s_{xx}} &= s_{xx}\left(\frac{\partial u}{\partial x}+\frac{\partial v}{\partial y}+\frac{\partial w}{\partial z}\right)\\ &\quad +2G\left(\frac{\partial u}{\partial x}-\Phi\right)+2(\Omega_{xy}s_{xy}+\Omega_{xz}s_{xz}),\end{aligned} \tag{4}$$

$$\begin{aligned}S_{s_{xy}} &= s_{xy}\left(\frac{\partial u}{\partial x}+\frac{\partial v}{\partial y}+\frac{\partial w}{\partial z}\right)+G\left(\frac{\partial u}{\partial y}+\frac{\partial v}{\partial x}\right)\\ &\quad +\Omega_{xy}(s_{yy}-s_{xx})+\Omega_{xz}s_{yz}+\Omega_{yz}s_{xz},\end{aligned} \tag{5}$$

$$\begin{aligned}S_{s_{xz}} &= s_{xz}\left(\frac{\partial u}{\partial x}+\frac{\partial v}{\partial y}+\frac{\partial w}{\partial z}\right)+G\left(\frac{\partial u}{\partial z}+\frac{\partial w}{\partial x}\right)\\ &\quad +\Omega_{xz}(s_{zz}-s_{xx})+\Omega_{xy}s_{yz}+\Omega_{zy}s_{xy},\end{aligned} \tag{6}$$

$$\begin{aligned}S_{s_{yy}} &= s_{yy}\left(\frac{\partial u}{\partial x}+\frac{\partial v}{\partial y}+\frac{\partial w}{\partial z}\right)+2G\left(\frac{\partial v}{\partial y}-\Phi\right)\\ &\quad +2(\Omega_{yx}s_{xy}+\Omega_{yz}s_{yz}),\end{aligned} \tag{7}$$

$$S_{s_{yz}} = s_{xz}\left(\frac{\partial u}{\partial x}+\frac{\partial v}{\partial y}+\frac{\partial w}{\partial z}\right)+G\left(\frac{\partial v}{\partial z}+\frac{\partial w}{\partial y}\right)$$

$$+\Omega_{yz}(s_{zz}-s_{yy})+\Omega_{yx}s_{xz}+\Omega_{zx}s_{xy}, \tag{8}$$

$$S_{s_{zz}} = s_{zz}\left(\frac{\partial u}{\partial x}+\frac{\partial v}{\partial y}+\frac{\partial w}{\partial z}\right) +2G\left(\frac{\partial w}{\partial z}-\Phi\right)+2(\Omega_{zx}s_{xz}+\Omega_{zy}s_{yz}), \tag{9}$$

where G is the shear modulus, $\Omega_{ij}=-\Omega_{ji}=\frac{1}{2}(\partial v_i/\partial x_j-\partial v_j/\partial x_i)$ is the component of the spin tensor, and $\Phi=\frac{1}{3}(\partial u/\partial x+\partial v/\partial y+\partial w/\partial z)$ is the volume strain.

By assuming that the temperature increase of the material is mainly caused by the plastic work, the incremental expression of the temperature is

$$\frac{\mathrm{d}T}{\mathrm{d}t}=\frac{\beta\dot{W}_{\mathrm{P}}}{\rho C}, \tag{10}$$

where C is the specific heat, and β is usually taken as 0.9. $\dot{W}_{\mathrm{P}}$ is the rate of the plastic work, which is approximated by

$$\dot{W}_{\mathrm{P}}\approx\dot{\varepsilon}^{\mathrm{p}}\sqrt{\frac{3}{2}S_{ij}S_{ij}}, \tag{11}$$

where $\dot{\varepsilon}^{\mathrm{p}}$ is the equivalent plastic strain rate and defined as

$$\dot{\varepsilon}^{\mathrm{p}}\approx\sqrt{\frac{2}{3}\dot{D}^{\mathrm{P}}_{ij}\dot{D}^{\mathrm{P}}_{ij}}, \tag{12}$$

with $\dot{D}^{\mathrm{P}}_{ij}$ being the plastic strain rate. According to Eqs. (11) and (12) , the source terms of the equivalent plastic strain and the temperature in Eq. (2) can be expressed as

$$S_{\varepsilon^{\mathrm{p}}}=\varepsilon^{\mathrm{p}}\left(\frac{\partial u}{\partial x}+\frac{\partial v}{\partial y}+\frac{\partial w}{\partial z}\right)+\sqrt{\frac{2}{3}\dot{D}^{\mathrm{P}}_{\mathrm{ij}}\dot{D}^{\mathrm{P}}_{ij}}, \tag{13}$$

$$S_T=T\left(\frac{\partial u}{\partial x}+\frac{\partial v}{\partial y}+\frac{\partial w}{\partial z}\right)+\frac{\beta\dot{W}_{\mathrm{P}}}{\rho C}. \tag{14}$$

The yield stress and the shear modulus are determined by the Johnson–Cook model[22] in the current work. The equivalent von Mises stress σ_{eq} is given by

$$\sigma_{\mathrm{eq}}=[A+B(\varepsilon^{P})^{n}][1+C\ln\dot{\varepsilon}^{*}][1-T^{*m}], \tag{15}$$

where A, B, C, n and m are the material constants; ε^{P} is the plastic strain; $\dot{\varepsilon}^{*}=\dot{\varepsilon}^{\mathrm{P}}/\dot{\varepsilon}_0$ is the dimensionless strain rate, with $\dot{\varepsilon}_0$ being a reference strain rate; and $T^{*}=(T-T_0)/(T_{\mathrm{m}}-T_0)$ the homologous temperature. Here, T is the actual temperature, T_0 is the room temperature and T_{m} is the melting temperature.

The Mie–Gruneisen equation of state is adopted here. The governing equations presented above can be used to describe high-velocity impact problems with large deformations and high strain rates. We will solve the equations using our newly developed high-resolution scheme.

3. The 3D CE/SE scheme

The space–time CE/SE method, originally devised by Chang,[11,12] is a novel numerical scheme used to solve the hyperbolic conservation laws. By treating space and time uniformly and introducing the concepts of the conservation element and solution element, the conservation laws are enforced locally and globally in both time and space. The spatial derivatives are also stored and calculated. In this way, the CE/SE method is compact and highly accurate.

In the present paper, the governing equations, Eq. (1), are 3D Euler equations with source terms. As the 3D CE/SE scheme[23] in Ref. [23] did not consider the source terms of the governing equations, a more complete 3D CE/SE scheme is given here.

For problems in three spatial dimensions (x, y, z), let $x_1=x$, $x_2=y$, $x_3=z$ and $x_4=t$ be considered as the coordinates of a four-dimensional (4D) Euclidean space, E_4. Simple types of SE and CE are defined for each grid point. For example, the conservation element CE(G') is defined by the 4D time-space region $A1A2A3A4A5A6A7A8A1'A2'A3'A4'A5'A6'A7'A8'$, and the solution element SE(G') is constituted by the four hexahedrons ($B1B3B11B9B1''B3''B11''B9''$, $B2B4B12B10B''2B4''B12''B10''$, $B5B6B7B8B5''B6''B7''B8''$, $A1'A2'A3'A4'A5'A6'A7'A8'$) intersecting at G'; see Fig. 1. If we suppose that the conservation equation (1) is satisfied in every CE, then the Gauss divergence theorem in spacetime E_4 implies that equation (1) can be rewritten as

$$\oiiint_{S(V)}\boldsymbol{H}\cdot\mathrm{d}\boldsymbol{s}=\iiint_{V(\mathrm{CE})}S(Q)\mathrm{d}x\mathrm{d}y\mathrm{d}z\mathrm{d}t,$$
$$\boldsymbol{H}=(Q,E,F,G),\quad \mathrm{d}\boldsymbol{s}=\mathrm{d}s\cdot\boldsymbol{n}, \tag{16}$$

where $S(V)$ is the boundary of the space–time volume CE, $\boldsymbol{H}$ is the space–time flux vector, $\boldsymbol{n}$ is the outward unit normal vector, and $\mathrm{d}s$ is the volume of the boundary element of $S(V)$. The physical variables in each SE are approximated by first-order Taylor expansions. Equation (1) is equivalent to

$$Q_{G'}-\frac{\Delta t}{4}S_{G'}=\frac{1}{8}\left(\bar{Q}+\frac{\Delta t}{\Delta x}\bar{E}+\frac{\Delta t}{\Delta y}\bar{F}+\frac{\Delta t}{\Delta z}\bar{G}+\frac{\Delta t}{4}\bar{S}\right), \tag{17}$$

with

$$\bar{Q}=Q\left(\frac{\Delta x}{4},\frac{\Delta y}{4},\frac{\Delta z}{4},0\right)_{A1}+Q\left(-\frac{\Delta x}{4},\frac{\Delta y}{4},\frac{\Delta z}{4},0\right)_{A2} +Q\left(-\frac{\Delta x}{4},-\frac{\Delta y}{4},\frac{\Delta z}{4},0\right)_{A3}+Q\left(\frac{\Delta x}{4},-\frac{\Delta y}{4},\frac{\Delta z}{4},0\right)_{A4} +Q\left(\frac{\Delta x}{4},\frac{\Delta y}{4},-\frac{\Delta z}{4},0\right)_{A5}+Q\left(-\frac{\Delta x}{4},\frac{\Delta y}{4},-\frac{\Delta z}{4},0\right)_{A6} +Q\left(-\frac{\Delta x}{4},-\frac{\Delta y}{4},-\frac{\Delta z}{4},0\right)_{A7} +Q\left(\frac{\Delta x}{4},-\frac{\Delta y}{4},-\frac{\Delta z}{4},0\right)_{A8}, \tag{18}$$

$$\begin{aligned}\bar{E} = {} & E\left(0,\frac{\Delta y}{4},\frac{\Delta z}{4},\frac{\Delta t}{4}\right)_{A1} - E\left(0,\frac{\Delta y}{4},\frac{\Delta z}{4},\frac{\Delta t}{4}\right)_{A2} \\ & - E\left(0,-\frac{\Delta y}{4},\frac{\Delta z}{4},\frac{\Delta t}{4}\right)_{A3} + E\left(0,-\frac{\Delta y}{4},\frac{\Delta z}{4},\frac{\Delta t}{4}\right)_{A4} \\ & + E\left(0,\frac{\Delta y}{4},-\frac{\Delta z}{4},\frac{\Delta t}{4}\right)_{A5} - E\left(0,\frac{\Delta y}{4},-\frac{\Delta z}{4},\frac{\Delta t}{4}\right)_{A6} \\ & - E\left(0,-\frac{\Delta y}{4},-\frac{\Delta z}{4},\frac{\Delta t}{4}\right)_{A7} \\ & + E\left(0,-\frac{\Delta y}{4},-\frac{\Delta z}{4},\frac{\Delta t}{4}\right)_{A8}, \end{aligned} \tag{19}$$

$$\begin{aligned}\bar{F} = {} & F\left(\frac{\Delta x}{4},0,\frac{\Delta z}{4},\frac{\Delta t}{4}\right)_{A1} + F\left(-\frac{\Delta x}{4},0,\frac{\Delta z}{4},\frac{\Delta t}{4}\right)_{A2} \\ & - F\left(-\frac{\Delta x}{4},0,\frac{\Delta z}{4},\frac{\Delta t}{4}\right)_{A3} - F\left(\frac{\Delta x}{4},0,\frac{\Delta z}{4},\frac{\Delta t}{4}\right)_{A4} \\ & + F\left(\frac{\Delta x}{4},0,-\frac{\Delta z}{4},\frac{\Delta t}{4}\right)_{A5} + F\left(-\frac{\Delta x}{4},0,-\frac{\Delta z}{4},\frac{\Delta t}{4}\right)_{A6} \\ & - F\left(-\frac{\Delta x}{4},0,-\frac{\Delta z}{4},\frac{\Delta t}{4}\right)_{A7} \\ & - F\left(\frac{\Delta x}{4},0,-\frac{\Delta z}{4},\frac{\Delta t}{4}\right)_{A8}, \end{aligned} \tag{20}$$

$$\begin{aligned}\bar{G} = {} & G\left(\frac{\Delta x}{4},\frac{\Delta y}{4},0,\frac{\Delta t}{4}\right)_{A1} + G\left(-\frac{\Delta x}{4},\frac{\Delta y}{4},0,\frac{\Delta t}{4}\right)_{A2} \\ & + G\left(-\frac{\Delta x}{4},-\frac{\Delta y}{4},0,\frac{\Delta t}{4}\right)_{A3} + G\left(\frac{\Delta x}{4},-\frac{\Delta y}{4},0,\frac{\Delta t}{4}\right)_{A4} \\ & - G\left(\frac{\Delta x}{4},\frac{\Delta y}{4},0,\frac{\Delta t}{4}\right)_{A5} - G\left(-\frac{\Delta x}{4},\frac{\Delta y}{4},0,\frac{\Delta t}{4}\right)_{A6} \\ & - G\left(-\frac{\Delta x}{4},-\frac{\Delta y}{4},0,\frac{\Delta t}{4}\right)_{A7} \\ & - G\left(\frac{\Delta x}{4},-\frac{\Delta y}{4},0,\frac{\Delta t}{4}\right)_{A8}, \end{aligned} \tag{21}$$

$$\bar{S} = S_{A1} + S_{A2} + S_{A3} + S_{A4} + S_{A5} + S_{A6} + S_{A7} + S_{A8}. \tag{22}$$

Here, $X(\mathrm{d}x,\mathrm{d}y,\mathrm{d}z,\mathrm{d}t)_N$ is the Taylor expansion at the reference point N, i.e.,

$$\begin{aligned} & X(\mathrm{d}x,\mathrm{d}y,\mathrm{d}z,\mathrm{d}t)_N \\ = {} & X_N + (X_x)_N\mathrm{d}x + (X_y)_N\mathrm{d}y + (X_z)_N\mathrm{d}z + (X_t)_N\mathrm{d}t. \end{aligned} \tag{23}$$

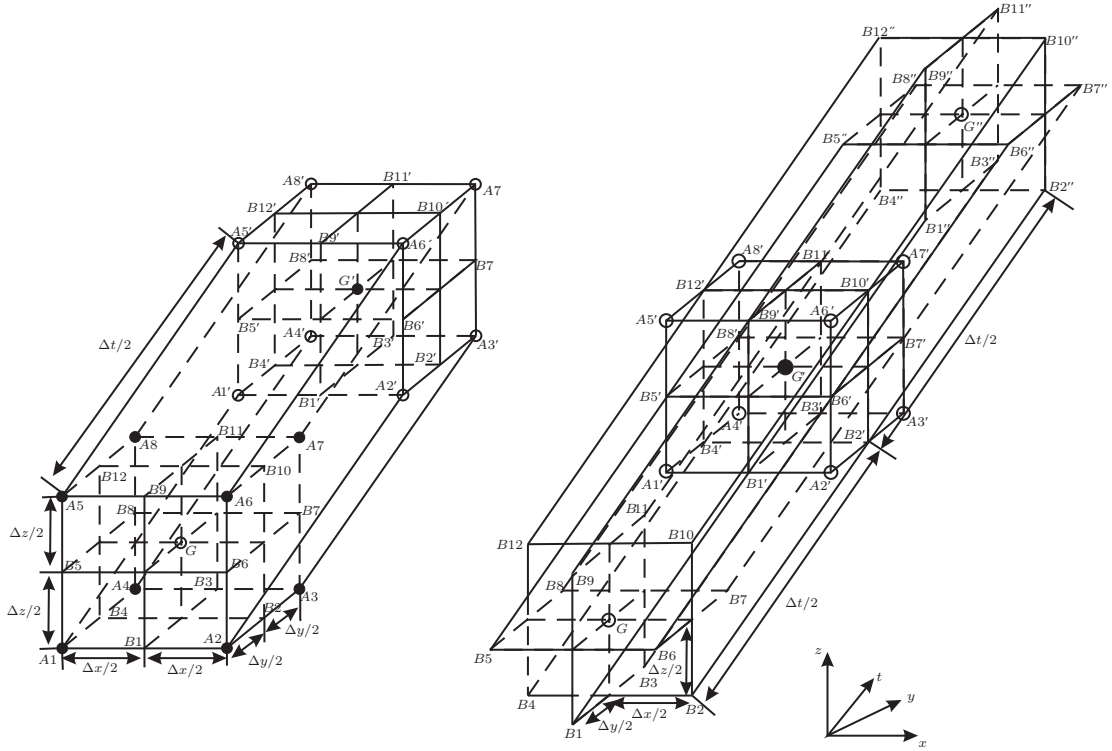


Fig. 1. Definitions of CE and SE for the improved three-dimensional CE/SE scheme: (a) CE(G'), (b) SE(G').

Using the continuous conditions at points $A1'$–$A8'$, we have the derivatives of Q with respect to x, y and z

$$\begin{aligned} (Q_x)_{G'} &= W[(Q_x)^-_{G'},(Q_x)^+_{G'},\alpha], \\ (Q_y)_{G'} &= W[(Q_y)^-_{G'},(Q_y)^+_{G'},\alpha], \\ (Q_z)_{G'} &= W[(Q_z)^-_{G'},(Q_z)^+_{G'},\alpha], \end{aligned} \tag{24}$$

where

$$\begin{aligned} & (Q_x)^-_{G'} \\ = {} & -\frac{1}{2\Delta x}\left[Q\left(0,0,0,\frac{\Delta t}{2}\right)_{A1} + Q\left(0,0,0,\frac{\Delta t}{2}\right)_{A4}\right. \\ & \left. + Q\left(0,0,0,\frac{\Delta t}{2}\right)_{A5} + Q\left(0,0,0,\frac{\Delta t}{2}\right)_{A8} - 4Q_{G'}\right], \end{aligned} \tag{25}$$

$$
\begin{aligned}
&(Q_x)^{+}_{G'}\\
&= +\frac{1}{2\Delta x}\left[Q\left(0,0,0,\frac{\Delta t}{2}\right)_{A2}+Q\left(0,0,0,\frac{\Delta t}{2}\right)_{A3}\right.\\
&\left.+Q\left(0,0,0,\frac{\Delta t}{2}\right)_{A6}+Q\left(0,0,0,\frac{\Delta t}{2}\right)_{A7}-4Q_{G'}\right], \quad (26)\\
&(Q_y)^{-}_{G'}\\
&= -\frac{1}{2\Delta y}\left[Q\left(0,0,0,\frac{\Delta t}{2}\right)_{A1}+Q\left(0,0,0,\frac{\Delta t}{2}\right)_{A2}\right.\\
&\left.+Q\left(0,0,0,\frac{\Delta t}{2}\right)_{A5}+Q\left(0,0,0,\frac{\Delta t}{2}\right)_{A6}-4Q_{G'}\right], \quad (27)\\
&(Q_y)^{+}_{G'}\\
&= +\frac{1}{2\Delta y}\left[Q\left(0,0,0,\frac{\Delta t}{2}\right)_{A3}+Q\left(0,0,0,\frac{\Delta t}{2}\right)_{A4}\right.\\
&\left.+Q\left(0,0,0,\frac{\Delta t}{2}\right)_{A7}+Q\left(0,0,0,\frac{\Delta t}{2}\right)_{A8}-4Q_{G'}\right], \quad (28)\\
&(Q_z)^{-}_{G'}\\
&= -\frac{1}{2\Delta z}\left[Q\left(0,0,0,\frac{\Delta t}{2}\right)_{A1}+Q\left(0,0,0,\frac{\Delta t}{2}\right)_{A2}\right.\\
&\left.+Q\left(0,0,0,\frac{\Delta t}{2}\right)_{A3}+Q\left(0,0,0,\frac{\Delta t}{2}\right)_{A4}-4Q_{G'}\right], \quad (29)\\
&(Q_z)^{+}_{G'}\\
&= +\frac{1}{2\Delta z}\left[Q\left(0,0,0,\frac{\Delta t}{2}\right)_{A5}+Q\left(0,0,0,\frac{\Delta t}{2}\right)_{A6}\right.\\
&\left.+Q\left(0,0,0,\frac{\Delta t}{2}\right)_{A7}+Q\left(0,0,0,\frac{\Delta t}{2}\right)_{A8}-4Q_{G'}\right]. \quad (30)
\end{aligned}
$$

The weighted average function is defined as

$$W(f_-,f_+,\chi)=\frac{|f_+|^{\chi}f_-+|f_-|^{\chi}f_+}{|f_+|^{\chi}+|f_-|^{\chi}}, \quad (31)$$

where χ is an adjustable constant, which usually equals 1–2.

As $S_{G'}$ is a function of $Q_{G'}$, a local Newton iterative procedure is usually needed to determine $S_{G'}$. In the present work, in order to save computation time, we replace $S_{G'}$ with its linear prediction of current time in Eq. (17), i.e.,

$$
\begin{aligned}
Q_{G'} &= \frac{1}{8}\left(\bar{Q}+\frac{\Delta t}{\Delta x}\bar{E}+\frac{\Delta t}{\Delta y}\bar{F}+\frac{\Delta t}{\Delta z}\bar{G}\right)+\frac{\Delta t}{32}\bar{S}+\frac{\Delta t}{4}\tilde{S}_{G'},\\
\tilde{S}_{G'} &= \frac{1}{8}\left(\bar{S}+\frac{\Delta t}{2}\bar{S}_t\right), \quad (32)
\end{aligned}
$$

where $\bar{S}_t$ is the time derivative of $\bar{S}$.

4. Interface capturing algorithm

In this work, a particle level set[24] formulation is used to capture the moving boundaries. We adopt different level set functions to describe different material interfaces. The governing equations for each material are solved, respectively, in the region $\varphi(\boldsymbol{x},t)<0$ of each level set function, and the level set functions are then reevaluated according to the material velocity fields.

The particle level set method[6] is a combination of a Eulerian level set method and a particle-based Lagrangian scheme. The positive- and negative-type particles are seeded randomly near the interface and attracted to the correct sides of the interface (positive for $\varphi>0$ and negative for $\varphi<0$). The particles are advected with the evolution equation

$$\frac{\mathrm{d}\boldsymbol{x}_{\mathrm{p}}}{\mathrm{d}t}=\boldsymbol{u}(\boldsymbol{x}_{\mathrm{p}}), \quad (33)$$

where $\boldsymbol{x}_{\mathrm{p}}$ is the position of the particle and $\boldsymbol{u}(\boldsymbol{x}_{\mathrm{p}})$ is the particle velocity. After each time step, the marker particles are employed to the correct possible errors in the level set function due to the non-physical deletion of the merging characteristics. The level set function of each particle is determined by the local interpolation of the surrounding grid points.

The particle level set method is shown to maintain the sharp corners of objects without excessive smoothing due to the inherent entropy fix in the advection scheme used to evolve the narrow-band grid-based level set. The particle level set method has been described in detail in previous papers.[6,24]

5. Boundary conditions

The mesh points that are out of the region of the material but are needed during the computation process are defined as the boundary points. The CE/SE scheme needs only one boundary point at each (x, y or z) direction. All boundary points can be classified into contact and free boundary points. The former describes the interaction between two material blocks, and the latter describes the movement of the free surface in vacuum. A mesh point is identified as the contact boundary point if it is a boundary point of a certain material and is located in the other material, and it is the free boundary point if it is a boundary point of one material and is not located in any other materials.

In previous works,[10,13,20] the values of the boundary points of a material were obtained via the GFM method. While the essential idea of the GFM is general, the specifics of implementation are important in determining its ability to provide physically correct solutions. In order to treat the elasto-plastic material interactions better, a modified GFM is proposed here.

5.1. Original GFM

The first step in assigning values to a boundary point P (see Fig. 2) is to obtain the interpolated values at R_P. Point R_P is obtained by reflecting the location of point P across the interface along the normal to the interface

$$\boldsymbol{x}_I=\boldsymbol{x}_P-|\varphi_P|\boldsymbol{n}, \quad (34)$$

$$\boldsymbol{x}_{RP}=\boldsymbol{x}_P-2|\varphi_P|\boldsymbol{n}, \quad (35)$$

where $\boldsymbol{x}$ is the position vector, φ_P is the level-set value at node P, and $\boldsymbol{n}$ is the normal vector at node P

$$\boldsymbol{n} = \frac{\nabla\varphi}{|\nabla\varphi|}. \tag{36}$$

A bilinear interpolation method is used to obtain the values at point R_P.

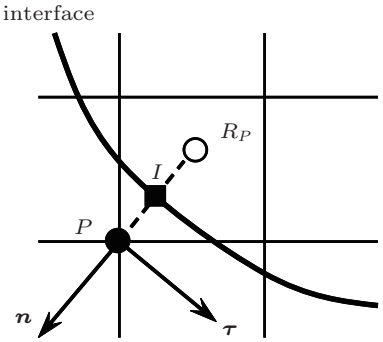


Fig. 2. Illustration of the boundary conditions.

The dependent variables at node R_P (Fig. 2) are transformed to those of the local normal and tangential coordinates. In 3D problems, the velocity components in the transformed coordinates are computed as follows:

$$u_n = \boldsymbol{u}\cdot\boldsymbol{n}, \quad u_{t1} = \boldsymbol{u}\cdot\boldsymbol{t}_1, \quad u_{t2} = \boldsymbol{u}\cdot\boldsymbol{t}_2, \tag{37}$$

where $\boldsymbol{u}$ is the velocity vector in the Cartesian coordinates, and u_n, u_{t1} and u_{t2} are the normal and tangential velocities, respectively. Suppose

$$\boldsymbol{n} = (n_x, n_y, n_z), \tag{38}$$

then

$$\boldsymbol{t}_1 = \frac{\boldsymbol{n}\times(1,0,0)}{|\boldsymbol{n}\times(1,0,0)|}, \quad \boldsymbol{t}_2 = \boldsymbol{n}\times\boldsymbol{t}_1. \tag{39}$$

The total stress tensor in the normal and tangential coordinates is given by

$$\tilde{\boldsymbol{\sigma}} = \boldsymbol{A}\boldsymbol{\sigma}\boldsymbol{A}^{\mathrm{T}}, \tag{40}$$

where

$$\boldsymbol{\sigma} = \begin{pmatrix} s_{xx}-p & s_{xy} & s_{xz} \\ s_{xy} & s_{yy}-p & s_{yz} \\ s_{xz} & s_{yz} & s_{zz}-p \end{pmatrix},$$
$$\boldsymbol{A} = \begin{pmatrix} n_x & n_y & n_z \\ t_{1x} & t_{1y} & t_{1z} \\ t_{2x} & t_{2y} & t_{2z} \end{pmatrix}. \tag{41}$$

If node P lies in the void region, then

$$u^{\mathrm{G}}_{n,P} = u_{n,RP}, \quad u^{\mathrm{G}}_{t1,P} = u_{t1,RP}, \quad u^{\mathrm{G}}_{t2,P} = u_{t2,RP}, \tag{42}$$
$$\tilde{\sigma}^{\mathrm{G}}_{nn,P} = -\tilde{\sigma}_{nn,RP}, \quad \tilde{\sigma}^{\mathrm{G}}_{nt1,P} = -\tilde{\sigma}_{nt1,RP},$$
$$\tilde{\sigma}^{\mathrm{G}}_{nt2,P} = -\tilde{\sigma}_{nt2,RP}, \tag{43}$$
$$\tilde{\sigma}^{\mathrm{G}}_{t1t1,P} = \tilde{\sigma}_{t1t1,RP}, \quad \tilde{\sigma}^{\mathrm{G}}_{t1t2,P} = \tilde{\sigma}_{t1t2,RP},$$
$$\tilde{\sigma}^{\mathrm{G}}_{t2t2,P} = \tilde{\sigma}_{t2t2,RP}, \tag{44}$$

where subscripts P and RP denote the values at points P and R_P, respectively, and superscript G denotes that the values are ghost fluid values. All other variables, such as the density and the internal energy computed at node R_P, are copied to the boundary point P.

If node P lies in another material, such as material 2, and if point P is tagged as a colliding node, then

$$u^{\mathrm{G}}_{n,P} = u_{n,P}, \quad u^{\mathrm{G}}_{t1,P} = u_{t1,RP}, \quad u^{\mathrm{G}}_{t2,P} = u_{t2,RP}, \tag{45}$$
$$\tilde{\sigma}^{\mathrm{G}}_{nn,P} = \tilde{\sigma}_{nn,P}, \quad \tilde{\sigma}^{\mathrm{G}}_{nt1,P} = \tilde{\sigma}_{nt1,P}, \quad \tilde{\sigma}^{\mathrm{G}}_{nt2,P} = \tilde{\sigma}_{nt2,P}, \tag{46}$$
$$\tilde{\sigma}^{\mathrm{G}}_{t1t1,P} = \tilde{\sigma}_{t1t1,RP}, \quad \tilde{\sigma}^{\mathrm{G}}_{t1t2,P} = \tilde{\sigma}_{t1t2,RP},$$
$$\tilde{\sigma}^{\mathrm{G}}_{\mathrm{t2t2,P}} = \tilde{\sigma}_{t2t2,RP}, \tag{47}$$

where $u_{n,P}$ is the normal velocity at point P in another material, such as material 2, $\tilde{\sigma}_{nn,P}$, $\tilde{\sigma}_{nt1,P}$, and $\tilde{\sigma}_{nt2,P}$ are the stress components at point P in material 2. All other variables, such as the density and the internal energy computed at node R_P are copied to the boundary point P. Equations (45)–(47) show that the normal velocity and the normal stress components crossing the interface between the two materials are continuous, whereas the tangential velocity and the tangential stress components may remain discontinuous.

5.2. Modified GFM

A 1D analysis is given to provide some insight into the GFM. Figure 3 shows the problem of material 1 impacting on material 2. The densities, velocities and stresses of materials 1 and 2 are ρ_1, u_1, σ_1 and ρ_2, u_2, σ_2, respectively, and in this case we assume $u_1 > u_2$. Point i is in material 1 and is also a boundary point of material 2. Similarly, point $i+1$ is in material 2 and is also a boundary point of material 1. In the simulation, the ghost fluid values at nodes i and $i+1$ can be given by the GFM. If we use the original GFM, the ghost fluid values at node i are ρ_2, u_1, σ_1, and the ghost fluid values at node $i+1$ are ρ_1, u_2 and σ_2. The ghost fluid momenta at nodes i and $i+1$ are $\rho_2 u_1$ and $\rho_1 u_2$, respectively. The total momentum at the boundary of the whole system is $\rho_1 u_2 + \rho_2 u_1$, which is different from the actual value $\rho_1 u_1 + \rho_2 u_2$. This will violate the conservation of momentum. Moreover, if

$$\rho_1 > \rho_2, \tag{48}$$

then

$$\rho_1 u_2 + \rho_2 u_1 < \rho_1 u_1 + \rho_2 u_2. \tag{49}$$

This means that the original GFM will cause a loss of momentum. In contrast, if

$$\rho_1 < \rho_2, \tag{50}$$

then

$$\rho_1 u_2 + \rho_2 u_1 > \rho_1 u_1 + \rho_2 u_2. \tag{51}$$

This means that the original GFM will cause an increase in momentum.

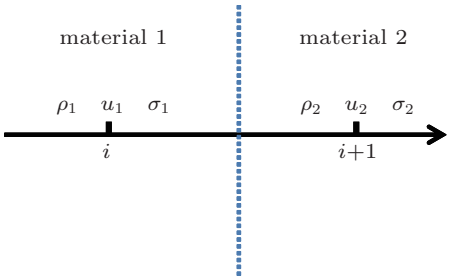


Fig. 3. The 1D impact problem.

In the present paper, in order to conserve the system momentum, the ghost fluid velocity values at nodes i and $i+1$ are both set to be

$$u^{\mathrm{G}} = \frac{\rho_1 u_1 + \rho_2 u_2}{\rho_1 + \rho_2}, \tag{52}$$

$$u_i^{\mathrm{G}} = u^{\mathrm{G}}, \tag{53}$$

$$u_{i+1}^{\mathrm{G}} = u^{\mathrm{G}}, \tag{54}$$

where u_i^{G} and u_{i+1}^{G} are the ghost fluid velocities at nodes i and $i+1$, respectively. The densities at ghost fluid nodes i and $i+1$ are ρ_2 and ρ_1, respectively. The impact problem shown in Fig. 3 can be considered as a Riemann problem (see Fig. 4). Then

$$\sigma_m - \sigma_1 = \rho_1 C_1 (u_m - u_1), \tag{55}$$

$$\sigma_m - \sigma_2 = -\rho_2 C_2 (u_m - u_2), \tag{56}$$

$$\sigma_m = \frac{\rho_1 C_1 \sigma_2 + \rho_2 C_2 \sigma_1 - \rho_1 C_1 \rho_2 C_2 (u_1 - u_2)}{\rho_1 C_1 + \rho_2 C_2}, \tag{57}$$

where σ_m and u_m are the stress and the velocity at node m, and C_1 and C_2 are the wave speeds of materials 1 and 2. The ghost fluid stress value at node $i+1$ can be extrapolated linearly from those at points i and m. Similarly, the ghost fluid stress value at node i can be extrapolated linearly from those at points $i+1$ and m

$$\sigma_i^{\mathrm{G}} = 2\sigma_m - \sigma_2, \tag{58}$$

$$\sigma_{i+1}^{\mathrm{G}} = 2\sigma_m - \sigma_1, \tag{59}$$

where σ_i^{G} and $\sigma_{i+1}^{\mathrm{G}}$ are the ghost fluid stresses at nodes i and $i+1$, respectively.

In 3D problems, the normal velocity and the normal stress components at the boundary points will be computed by the modified GFM described above, whereas the other values will be computed by the original GFM.

A test is implemented for both the original GFM and the modified GFM. The problem that a 6061-T651 aluminum target plate is impacted by a spherical 4340 steel projectile at a velocity of 400 m/s is simulated. The length, width and height of the target plate are 20 mm, 20 mm and 10 mm, respectively, and the diameter of the projectile is 5 mm. A geometrical sketch of the high-velocity impact problem is illustrated in Fig. 5. The mesh size is 0.333 mm×0.333 mm×0.333 mm.

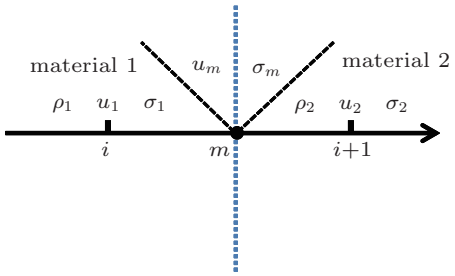


Fig. 4. A 1D Riemann problem.

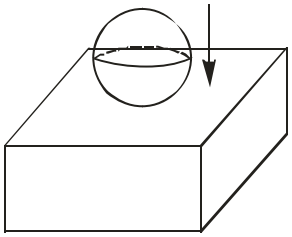


Fig. 5. A geometrical sketch of a high-velocity impact problem.

In order to investigate the influence of the GFM on the momentum of the system, the problem is simulated by both models with the original GFM and the modified GFM. Figure 6 presents the time histories of the momenta of different parts of the system. We monitored the momentum and output the value at a time interval of 1 μs. In Figs. 6 and 7, p_1, p_{p1} and p_{t1}. These are simulated with the original GFM and are the momenta of the whole system, the projectile and the target, respectively. p_2, p_{p2} and p_{t2} are also the momenta of the whole system, the projectile and the target, respectively, but are simulated with the modified GFM. The exact momentum of the whole system is p_{exact}. According to the law of the conservation of momentum, the momentum of the whole system should be a constant and equal to p_{exact} in Fig. 6. It is observed that the profile of p_2, which is simulated with the modified GFM, agrees well with p_{exact}, while the profile of p_1, which is simulated with the original GFM, is lower than that of p_{exact}. In this case, as the density of steel is higher than that of aluminum, then the loss of momentum caused by the original GFM is predicted by Eq. (49).

In order to further validate the influence of the GFM on the momentum of the system, another problem where a copper target plate is impacted by a spherical 6061-T651 aluminum projectile at a velocity of 400 m/s is simulated. The length, width and height of the target plate are 20 mm, 20 mm and 10 mm, respectively, and the diameter of the projectile is 5 mm. The mesh size is 0.333 mm×0.333 mm×0.333 mm. Figure 7 presents the time histories of the momenta of different parts of the system. It is observed that the profile of p_2, which is simulated with the modified GFM, agrees well with that of p_{exact}, while the profile of p_1, which is simulated with the original GFM, is higher than that of p_{exact}. In this case, as the density of aluminum is lower than that of copper, the increase in momentum caused by the original GFM is predicted by Eq. (51). The numerical tests show that the modified GFM can obtain an improved match between the simulation and the exact solution.

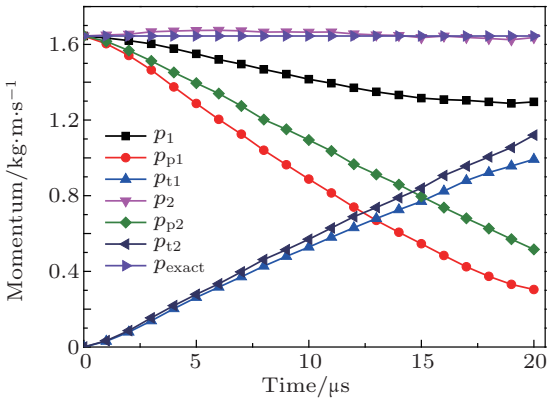


Fig. 6. (color online) The time histories of the momenta in the problem where a 6061-T651 aluminum target plate is impacted by a spherical 4340 steel projectile. Here, p_1, p_{p1} and p_{t1}, which are simulated with the original GFM, are the momenta of the whole system, the projectile and the target, respectively; p_2, p_{p2} and p_{t2} are also the momenta of the whole system, the projectile and the target, respectively, whereas they are simulated with the modified GFM; and p_{exact} is the exact momentum of the whole system.

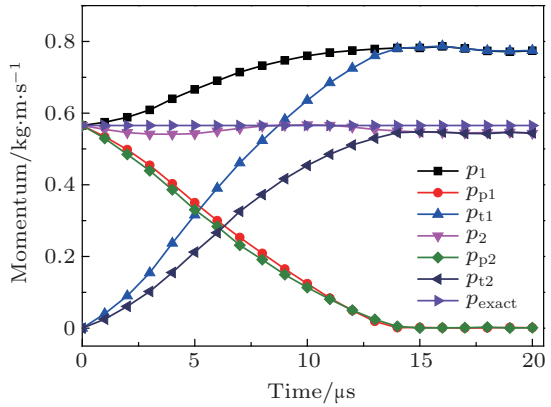


Fig. 7. (color online) The time histories of the momenta in the problem where a copper target plate is impacted by a spherical 6061-T651 aluminum projectile. Here, p_1, p_{p1} and p_{t1}, which are simulated with the original GFM, are the momenta of the whole system, the projectile and the target, respectively; p_2, p_{p2} and p_{t2} are also the momenta of the whole system, the projectile and the target, respectively, whereas they are simulated with the modified GFM; and p_{exact} is the exact momentum of the whole system.

6. Application

This section presents two numerical examples to demonstrate the applicability and performance of our 3D computational technique. The present scheme is implemented on parallel distributed-memory computers using a domain-decomposition approach. The inter-processor communication is handled using the MPI library.

6.1. Taylor bar impact

The famous Taylor bar impact problem where a cylindrical copper bar impacts on a rigid and frictionless wall is simulated. The radius and length of the copper cylinder are 3.2 mm and 32.4 mm, respectively, and the initial impact velocity is 227 m/s. The mechanical parameters of the copper bar used in the calculation are as follows: the initial density is 8930 kg/m^3; the elastic modulus is 117 GPa; the Poisson ratio is 0.35; and the yield strength is 400 MPa. The copper bar is modeled by the linear isotropic hardening constitutive model with tangent hardening modulus $E_{\text{t}} =$ 100 MPa. The computational domain consists of a cuboid of dimensions 16 mm×16 mm×37 mm. The mesh size is 0.15 mm×0.15 mm×0.15 mm, and the calculation is carried out up to 80 μs.

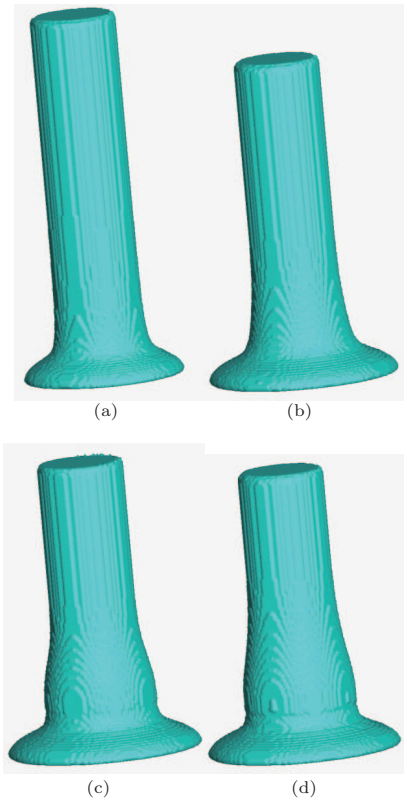


Fig. 8. (color online) The deformation of the copper bar at four different times: (a) 20 μs, (b) 40 μs, (c) 60 μs and (d) 80 μs.

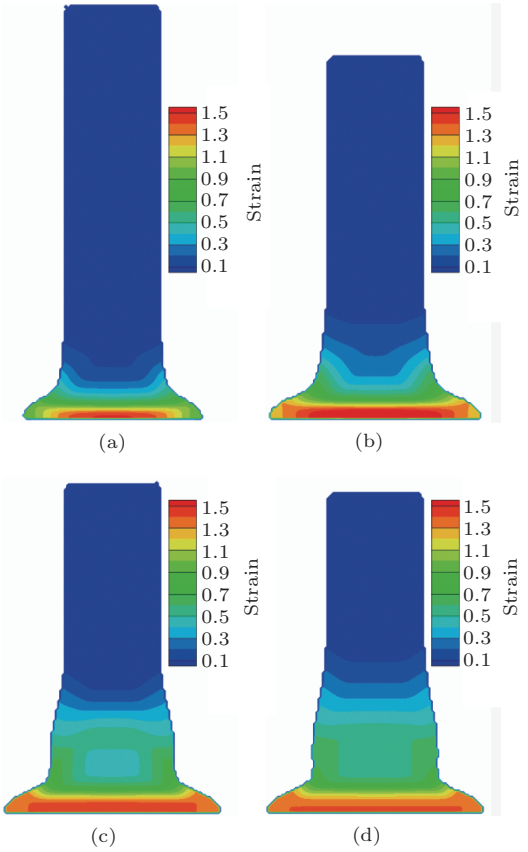


Fig. 9. (color online) The equivalent plastic strain contours at a cross-section of the Taylor bar at (a) 20 μs, (b) 40 μs, (c) 60 μs and (d) 80 μs.

Figure 8 shows the deformation of the copper bar at four different times: 20 μs, 40 μs, 60 μs and 80 μs. It is found that the jetting phenomenon continues until 40 μs (Fig. 8(b)), at which point the material begins to harden, resulting in the mushroom shape at the base of the material (Fig. 8(d)). The effective plastic strain at the cross section of the bar is shown in Fig. 9. The effective plastic strain is concentrated mostly at the base of the bar. The final maximum radius and the residual bar length are calculated by our 3D computational scheme, compared with the corresponding results from Paik *et al.*,[25] Hu *et al.*,[26] and Kapahi[8], and are listed in Table 1. It can be found that our results agree well with those in the references.

Table 1. A comparison of the results for the Taylor copper bar impact problem.

	Final length/mm	Final radius/mm
Our method	21.6	7.2
Paik *et al.*[25]	21.23	6.18
Hu *et al.*[26]	21.6	7.1
Kapahi[8]	21.8	6.36

6.2. Perforation and ricochet phenomena in thin plates

The real test of a 3D multimaterial code is to simulate impact phenomena at an angle. In this section, the perforation and ricochet of an SAE 52100 steel sphere impacting a 2024-T3 plate aluminum target at an angle of 60° are simulated. The experiment was conducted by Backman and Finnegan.[21] The initial velocity of the sphere is 729 m/s. The diameter of the SAE 52100 steel sphere is 6.35 mm, and the dimensions of the plate are 40 mm×30 mm×6.35 mm. The mesh size is 0.125 mm×0.125 mm×0.125 mm, and the material properties are given in Table 2.

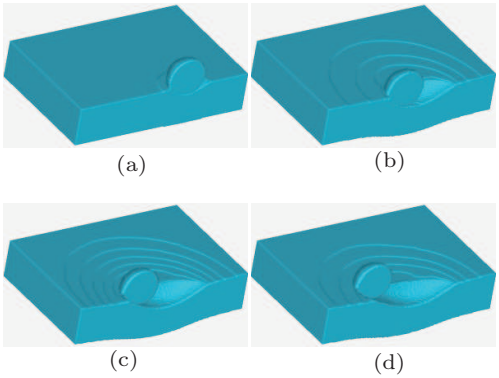


Fig. 10. (color online) The interface topology for the inclined (60°) impact of an SAE 52100 steel sphere on a 2024-T3 aluminum plate at 729 m/s, at (a) 5 μs, (b) 15 μs, (c) 25 μs and (d) 35 μs.

The interface topology at different times is shown in Fig. 10. It is observed that the sphere rebounds off the surface of the target and a ricochet phenomenon, which is also observed in the experiment,[21] occurs. The crater formed by the projectile is elliptical. The depth of the crater simulated by the present 3D scheme with the modified GFM is 2.625 mm. This result is in excellent agreement with the experimental value of 2.667 mm reported by Backman and Finnegan.[21] The computed residual velocity of the projectile is 317 m/s, which is also in excellent agreement with the experimental value of 311 m/s.

The temperature distribution of the projectile and target at $t = 20$ μs after impact is presented in Fig. 11. In the zones near the projectile, the temperature rises significantly. The local adiabatic temperature rise will decrease the strength of the target material, and thus deformation of the target material easily occurs due to the softening effect.

The experiment is also simulated by the present 3D scheme with the original GFM. The crater depth and the residual velocity computed with the original GFM are 2.25 mm and 373 m/s, respectively. According to the experimental data, these results are not as good as those computed with the modified GFM.



Fig. 11. (color online) The temperature distribution of the projectile and target at $t = 20$ μs.

Table 2. Material model parameters with reference to Eq. (15).

Material	A/Gpa	B/Gpa	n	C	m	G/Gpa	T_m/K
SAE 52100 steel[27]	0.35	1.498	0.19	0.027	0.66	80	1720
2024-T3 aluminum[28]	0.369	0.684	0.73	0.0083	1.7	28	775

7. Conclusion

In this paper, an innovative computational methodology is proposed to simulate 3D high-velocity impact problems. A more complete 3D CE/SE scheme is provided. The GFM implemented in solid–solid interfaces is modified to treat the boundary conditions at the interfaces. It is proved that a better agreement with the experiment is obtained when the modified GFM is adopted. Numerical simulations of a Taylor bar problem and the ricochet phenomenon of a sphere impacting a plate target at an angle of 60° are carried out. The simulation results are in good agreement with the experimental data.

References

[1] Goldsmith W 1999 *Int. J. Impact Eng.* **22** 95
[2] Anderson C E 1987 *Int. J. Impact Eng.* **5** 33
[3] Ma S, Zhang X, Lian Y P and Zhou X 2009 *Cmes. Comp. Model. Eng.* **39** 101
[4] Udaykumar H S, Tran L, Belk D M and Vanden K J 2003 *J. Comput. Phys.* **186** 136
[5] Tran L B and Udaykumar H S 2004 *J. Comput. Phys.* **193** 469
[6] Enright D, Fedkiw R, Ferziger J and Mitchell I 2002 *J. Comput. Phys.* **183** 83
[7] Kapahi A, Sambasivan S and Udaykumar H S 2013 *J. Comput. Phys.* **241** 308
[8] Sambasivan S, Kapahi A and Udaykumar H S 2013 *J. Comput. Phys.* **235** 334
[9] Barton P T, Deiterding R, Meiron D and Pullin D 2013 *J. Comput. Phys.* **240** 76
[10] Wang J T, Liu K X and Zhang D L 2009 *Comput. Fluids* **38** 544
[11] Chang S C 1995 *J. Comput. Phys.* **119** 295
[12] Chang S C, Wang X Y and Chow C Y 1999 *J. Comput. Phys.* **156** 89
[13] Chen Q Y, Wang J T and Liu K X 2010 *J. Comput. Phys.* **229** 7503
[14] Chen Q Y and Liu K X 2011 *Chin. Phys. Lett.* **28** 064602
[15] Fedkiw R P, Aslam T, Merriman B and Osher S 1999 *J. Comput. Phys.* **152** 457
[16] Sambasivan S and Udaykumar H S 2009 *AIAA* **47** 2907
[17] Sambasivan S and Udaykumar H S 2009 *AIAA* **47** 2923
[18] Liu T G, Khoo B C and Yeo K S 2003 *J. Comput. Phys.* **190** 651
[19] Barton P T and Drikakis D 2010 *J. Comput. Phys.* **229** 5518
[20] Chen Q Y and Liu K X 2012 *Comput. Fluids* **56** 92
[21] Backman M E and Finnegan S A 1976 *Naval Weapons Center*
[22] Johnson G R and Cook W H 1983 *7th Int. Symp. on Ballistics* (Hague, Netherlands)
[23] Shen H, Liu K X and Zhang D L 2011 *Chin. Phys. Lett.* **28** 124705
[24] Osher S and Fedkiw R P 2001 *J. Comput. Phys.* **169** 463
[25] Paik S H, Moon J, Kim S J and Lee M 2006 *Computers & Structures* **84** 732
[26] Hu W, Yao L G and Hua Z Z 2007 *Engineering Analysis with Boundary Elements* **31** 326
[27] Yue C X, Liu X L, Jia D K, Ji S Y and Zhai Y S 2009 *Advanced Materials Research* **69–70** 11
[28] Lesuer D R 2000 *FAA report DOT/FAA/AR-00/25*